Journal of Materials Research and Technology 36 (2025) 358–368

Contents lists available at ScienceDirect

Journal of Materials Research and Technology

journal homepage: www.elsevier.com/locate/jmrt

Reinforcement of injectable hydrogels through melt electro-written structures: Influence of shape and pore size on the injection force

Diego Trucco [a,b,c,*], Rory Gibney [d,e], Lorenzo Vannozzi [a,b], Gina Lisignoli [c], Daniel J. Kelly [d,e], Leonardo Ricotti [a,b]

[a] The BioRobotics Institute, Scuola Superiore Sant'Anna, Piazza Martiri Della Libertà 33, Pisa, 56127, Italy
[b] Department of Excellence in Robotics & AI, Scuola Superiore Sant'Anna, Piazza Martiri Della Libertà 33, Pisa, 56127, Italy
[c] IRCCS Istituto Ortopedico Rizzoli, SC Laboratorio di Immunoreumatologia e Rigenerazione Tissutale, Via di Barbiano, 1/10, Bologna, 40136, Italy
[d] Trinity Centre for Biomedical Engineering, Trinity Biomedical Sciences Institute, Trinity College, Dublin, Ireland
[e] Department of Mechanical, Manufacturing and Biomedical Engineering, School of Engineering, Trinity College, Dublin, Ireland

ARTICLE INFO

Handling editor: P.Y. Chen

Keywords:
Melt electro-writing
Reinforced hydrogel
PCL
Injectable hydrogel
Tissue engineering

ABSTRACT

Hydrogels are commonly used for tissue engineering applications due to their high water content, biocompatibility, injectability, and ability to mimic the extracellular matrix of native tissues. However, their weak mechanical properties limit their use, especially in load-bearing applications. In this study, we developed fibrous architectures with a pre-defined shape using melt electro-writing (MEW) to strengthen injectable hydrogels. We assessed the injection forces required to successfully extrude the hydrogel reinforced with MEW-printed structures, varying their geometry (square/hexagonal pores) and pore sizes (0.6, 0.8, 1.0 mm) through needles having a size compatible with clinical applications. Our findings indicate that MEW structures with hexagonal pores exhibit a higher tensile modulus than those with square pores. Additionally, the injection forces required to extrude hydrogels embedding MEW structures through needles were greater for hexagonal pores. Thinner pores and smaller needle diameters resulted in higher injection forces; a few conditions among the ones tested were compatible with the limits defined by the EU ISO 7886–1:2018 standard. After injection and crosslinking, hydrogels reinforced with MEW structures showed improved mechanical properties (up to 6.34-fold), particularly when structures with hexagonal pores were used.

1. Introduction

Hydrogels have emerged as promising materials in tissue engineering and regenerative medicine, due to their unique properties that comprise high water content, biocompatibility, injectability, and ability to mimic the extracellular matrix of native tissues, especially in the case of natural hydrogels [1,2]. However, their inherently low mechanical properties raise the need for reinforcements, to meet the mechanical demands of various biomedical applications, such as their use in load-bearing regions [3].

Different strategies have been pursued in the state-of-the-art to reinforce hydrogels, such as the use of blends or interpenetrating polymer networks [4–6], and the use of fillers (e.g., nanoparticles or fibers) [7–11].

An exciting approach that has emerged in recent years involves melt electro-writing (MEW) of fibrous structures or networks to reinforce soft hydrogels [9,12]. MEW is a 3D printing technology that offers precise control over the deposition of micrometer-scale fibers, overcoming the spatial resolution of other methods, such as fused deposition modeling. This technology enables the printing of micro and sub-micron fibers [13–17] using a high voltage between a print nozzle and a collector to stabilize the flow of the printing material, facilitating the controlled deposition of fibers following a pre-set pattern [18]. MEW has been explored for various tissue engineering applications [19,20], including the fabrication of complex anatomically relevant porous microarchitectures to engineer specific biological tissues [21–23]. Polycaprolactone (PCL) is a commonly used synthetic polymer in the field of tissue engineering due to its low melting temperature (around 60°C), biocompatibility, relatively slow degradation rate (2–3 years), and attractive mechanical properties [20,24–26]. PCL-based structures are commonly used to enhance the mechanical properties of hydrogels, acting as reinforcing structures that can better withstand compressive

* Corresponding author. Viale Rinaldo Piaggio, 34, Pontedera (PI), Italy.
E-mail address: diego.trucco@santannapisa.it (D. Trucco).

https://doi.org/10.1016/j.jmrt.2025.03.133
Received 11 December 2024; Accepted 15 March 2025
Available online 17 March 2025

and tensile forces [27]. Several studies have highlighted the potential of reinforced structures fabricated *ex-situ* by combining MEW fibrous networks with the printing or casting of hydrogels for several tissue types, including bone [28], cartilage [23], the osteochondral unit [29], or for wound healing [22]. These structures can also guide cells via geometrical cues [16,30], enabling the engineering of more structurally complex tissues.

At present, strengthening hydrogels through MEW structures is mainly pursued by developing these scaffolds outside the body and then implanting them. This approach requires open surgery, which has its limitations and lose the possibility of injecting the hydrogels directly in place using a minimally invasive procedure. Moreover, *ex situ*-printed or casted constructs hardly fit the site of interest once implanted (e.g., due to swelling or deformation) in the case of load-bearing applications like in articular cartilage [31]. An additional downside is the potential contamination during transportation, manual implantation, and suturing [32].

Recently, injectable hydrogels to reconstruct or repair damaged tissues adapting to anatomical constraints are gaining growing interest [33–35]. To date, the injectability of MEW structure-laden hydrogels has been only partly investigated. Castilho et al. [36] provided preliminary proof of injectability and shape recovery of cardiac patches made from ultra-stretchable microfiber MEW scaffolds with controlled hexagonal microstructures, demonstrating successful extrusion through a catheter-like tubing with a big inner diameter (Ø = 1.5 mm) within culture media. Wang et al. [37] explored the extrusion of a PCL-based MEW ultra-flexible conductive scaffold with a gold nanolayer, showcasing high flexibility and recoverability while reporting on the successful injection rate relative to the coating layer. Nahm et al. [38] visually demonstrated the injection of two-layer MEW structures made from hydrophilic poly(2-ethyl-2-oxazine) (PEtOzi) through a glass pipette within an aqueous medium, which exhibited good shape retention post-injection, although without measuring the injection forces.

Overall, no studies have quantified the injection force needed to extrude hydrogels embedding MEW structures. However, this is an important aspect since specific limits exist, as defined by the EU–ISO–7886–1:2018 standard, to enable the clinical translation of injectable hydrogels. Furthermore, the influence of shape and pore size on injectability force has not been clarified, so far.

In this paper we explored the injectability of MEW structures-laden hydrogels, by comparing square-shaped and hexagon-shaped pore designs, and three different pore sizes (0.6, 0.8, and 1.0 mm). We characterized these structures from a morphological and mechanical viewpoint, and we quantified the injection forces needed to extrude the MEW structures-laden hydrogels using needles of different sizes, compatible with the clinical use. Finally, we quantified the mechanical properties of the MEW-reinforced hydrogels after extrusion and subsequent hydrogel cross-linking, to verify the reinforcement level guaranteed by the presence of the MEW structures.

2. Materials and methods

2.1. Materials

GMP-grade polycaprolactone (PCL, CAPA-6500, Mw: 50 kDa) was purchased by Ingevity (USA). Sodium alginate (A, code n. W201502), gelatin from bovine skin (G, code n. G9382), calcium chloride ($CaCl_2$, code n. C1016), gellan gum (GG, trademarked as Gelzan^{CM}), methacrylic anhydride (MA), phosphate-buffered saline without Ca^{2+}/Mg^{2+} (PBS), tris(2,2′-bipyridyl) ruthenium (II) chloride hexahydrate (Ru), and sodium persulfate (SPS) were purchased by Merck (USA). Dialyzing membranes (MWCO 12–14 kDa) were purchased from CelluSep (USA). VitroGel-RGD® hydrogel (VG-RGD) and Dilution Solution Type 1® were purchased from Well Bioscience (North Brunswick, NJ, USA). Dulbecco Modified Eagle Medium (DMEM) (Life Technologies, Bleiswijk, Netherlands). Biopsy punches (diameter: 8 mm) were purchased by Kai Medical (Japan). Stainless steel needles (18G, 16G, and 14G) were purchased by Nordson (USA).

2.2. Melt electro-writing of PCL structures

PCL was loaded and extruded through a custom-made MEW printer [18] using 3 mL syringes with 22 G nozzles. The barrel and nozzle were maintained at 87.5°C and 92.5°C within the print head during the entire process. The syringe piston was pushed with an air pressure of 0.6 bar, and the printer head moved at a printing speed of 15 mm/s. An initial voltage of 6 kV was applied, with a collector distance of 5 mm. The voltage was increased by 0.0129 kV/layer, and the print head was increased by 22.7 μm/layer. The scaffolds (48 × 48 mm) were printed with 40 layers per structure, resulting in a ~1 mm height structure. Two pattern designs were investigated: a square pore size geometry, named GRID, consisting of alternating layers with vertical (0°) and horizontal (90°) fibers, and a hexagonal pore shape geometry, named HEX, with honeycomb pore sizes. The pore size of both pattern designs varied between 0.6, 0.8, and 1.0 mm. The pore size of GRID structures was measured as the distance between two consecutive fibers, while for HEX structures, it was determined as the radius of the circumscribed circle of the hexagon. After printing, the structures were removed from the printer bed and punched to a diameter of 8 mm using biopsy punches.

2.3. Hydrogels preparation

Gelatin (G) powder was dissolved in deionized water (d-H_2O) to achieve a concentration of 3 % w/v under magnetic stirring at 50°C for 1 h. Then, sodium alginate (A) powder was added to the solution to reach a final concentration of 3 % w/v and stirred for 2 h, keeping the temperature at 50°C. The AG blend solution (named A3G3 because each component was at 3 % w/v) was then cooled to 25°C until use.

2.4. Morphological and mechanical characterization of MEW structures

Microscopical images of MEW structures after printing were acquired through an inverted microscope (Olympus, XX) to evaluate the GRID and HEX design with different pore sizes. The porosity of MEW structures was calculated as reported in the Supplementary Materials (section "*Porosity of MEW structures*"), based on the single unit of the MEW structure shown in Fig. S1.

Punched MEW structures were covered by a thin Au layer using a Mini Sputter Coater (model SC7620, Quorum, UK) to visualize them with the scanning electron microscope (SEM, Phenom XL, Thermo Fisher, USA). An intensity of 15 mA was applied for 60 s to depose a thin film of ~5 nm in thickness under a sputter rate of 5 nm/min (at 15 mA) following the datasheet. Then, the structures were visualized via SEM under the high vacuum condition by setting a beam voltage of 5 kV.

Mechanical characterization in terms of compression and tensile modulus was performed through an Instron Mechanical Testing System (Instron, Norwood, MA, USA). Compression tests were performed with a displacement rate of 1 mm/mm until fracture on two staked punched structures to achieve a total height of ~2 mm [12]. Tension tests were performed on cut structures with a rectangular shape (25 x 10 × 1 mm) until fracture with a displacement rate of 1 mm/s. Compression and tensile moduli were extracted as the slope of the stress-strain curves. Stress was calculated as the ratio of the load (N) measured to the cross-sectional area. Four MEW structures were analyzed in terms of compression and tensile modulus.

2.5. Rheological characterization

The rheological characterization was carried out on the A3G3 hydrogel solution without embedding any MEW structure. All rheological tests were performed using a rheometer (Anton Paar MCR-302, Graz, Austria) with a cone-plate geometry (diameter: 50 mm, angle =

1°) on the solutions immediately after preparation. The flow curves were acquired at room temperature (25°C) at shear rates ranging from 0.1 to 1000 s^{-1} in rate-controlled mode by selecting 10 points for each decade. The viscosity was modeled as a non-Newtonian fluid according to the following power law [39]:

$$\eta = K\dot{\gamma}^{n-1} \quad (1)$$

where η is the dynamic viscosity, $\dot{\gamma}$ is the fluid shear rate, K is the consistency index and n is the flow behavior index. The rheological indexes were extracted from each curve and reported as mean ± standard deviation.

2.6. Injection of MEW structures

A custom setup was used with a 6 mL syringe and stainless-steel needles of varying diameters (18G, 16G, and 14G) to test the injectability of the hydrogel solutions. Each test involved the loading of one punched structure (8 mm diameter) in 2.5 mL of hydrogel solution into the syringe. The syringe's piston was then compressed using a 200 N load cell attached to a Zwick Mechanical Testing Machine (Zwick Roell, Ireland). All tests were performed with a displacement rate of 2.5 mm/s to measure the injection force. Results of the injection force tests were presented as the difference between the maximum peak force recorded during the flow of the MEW structure and the injection force value obtained when extruding the unreinforced hydrogel. Four MEW structures for each configuration were extruded to measure the injection forces within the hydrogel solution.

2.7. Mechanical characterization of MEW-reinforced hydrogel

Punched MEW structures with an 8 mm diameter for all configurations were added to a syringe containing the hydrogel and extruded into cylindrical molds to create reinforced hydrogels. The excess hydrogel solution was removed and then the MEW-reinforced hydrogels were ionically cross-linked with a 1 % w/v $CaCl_2$ solution in d-H_2O for 10 min after injection. The Ca^{2+} ions were able to penetrate through the whole 1 mm-thick reinforced hydrogel according to the model reported in Palma's study [40]. Controls were prepared by extruding just the hydrogel without embedding the MEW structure and ionically cross-linking. The cross-linked samples with and without the MEW structure as reinforcement were mechanically compressed until fracture using an Instron Mechanical Testing System (Instron, Norwood, MA, USA) with a displacement rate of 1 mm/mm. Compression moduli were extracted as the slope of the stress-strain curves, fracture strain and fracture stress were extracted at the fracture point of the stress-strain curves, and toughness values were the area under the stress-strain curves. Four MEW structures for each configuration needles within the hydrogel solution were extruded from 14G and cross-linked to evaluate the mechanical properties.

2.8. Impact of different hydrogels on MEW structure injection and mechanical properties of MEW-reinforced hydrogels

2.8.1. Preparation of VitroGel-RGD and methacrylated gellan gum (GGMA) hydrogels

The VitroGel-RGD® hydrogel (VG-RGD) was prepared following the manufacturer's protocol. Briefly, the VG-RGD hydrogel solution was directly mixed at room temperature (RT) with the manufacturer's Dilution Solution Type 1® at the ratio of 1:2. Then, DMEM was added to the pre-crosslinked solution at the ratio of 4:1 (pre-crosslinked solution: DMEM) at RT before use. We referred to the mixed hydrogel with VG-RGD.

Concerning methacrylated gellan gum (GGMA), the methacrylation procedure was performed similarly to previous works [41,42]. Briefly, gellan gum (GG) powder was dissolved in d-H_2O, (1 % w/v) with a magnetic stirrer at 75 °C for 1 h. Then, the solution was cooled to 60 °C, and 8.5 mL of MA per 100 mL of solution were slowly added. The solution reacted for 6 h at a controlled pH range (8–9), then was centrifuged (3500 rpm for 3 min) at 30°C to remove the unreacted MA, and the supernatant was diluted (1:2) with deionized water pre-heated at 40°C. The solution was dialyzed at 60°C for 5 days, quickly frozen, and stored at −80°C. Finally, aliquots were lyophilized (Labconco, FreeZone 2.5 Plus) for 3 days to obtain the GGMA powder and kept at −80°C before use. The GGMA powder was also autoclaved at a temperature of 120°C and a pressure of 1 bar for 30 min.

The GGMA hydrogel solution was obtained by dissolving the lyophilized autoclaved GGMA powder in PBS at 37°C in a water bath to achieve a concentration of 2 % w/v. Then, Ru (0.1×10^{-3} M) and SPS (1×10^{-3} M) were added to the GGMA solution to enable the matrix photo-crosslinking in response to light. Ru/SPS, used as photo-initiators, are featured by a high absorbance in the 400–500 nm range. Ru and SPS were previously prepared as 20×10^{-3} and 200×10^{-3} M stock solutions in d-H_2O, respectively.

2.8.2. Rheological characterization and injection of MEW structures

Both hydrogel solutions (VG-RGD and GGMA) were rheologically characterized without embedding any MEW structure following the protocol reported in section 2.5.

To verify the influence of different hydrogels on injection force, the structure design that resulted in the lowest injection force from the previous injection test within the A3G3 hydrogel solution (i.e., GRID structure with a 1.0 mm pore size) was incorporated into the VG-RGD and GGMA hydrogel solutions. Then, the injection tests were carried out following the same procedure reported in section 2.6.

2.8.3. Mechanical characterization

After the injection procedure, the hydrogel solutions were cross-linked as follows. Briefly, the VG-RGD hydrogel solution was left stabilizing for 20 min at RT after mixing with DMEM solution. The GGMA hydrogel solution was cross-linked using a white LED source (RfQ – Medizintechnik, GmbH & Co) for 60 s at an intensity of 18 mW/cm^2, applied at 1.5 cm from the top. Controls were also prepared by extruding each hydrogel without embedding the MEW structure. The same compression tests performed for A3G3 hydrogels and reported in section 2.7 were carried out. Then, the fold increase in compressive moduli between unreinforced and reinforced cross-linked hydrogels was calculated by dividing the moduli obtained with reinforcement by the average compressive modulus of unreinforced hydrogels.

2.9. Statistical analysis

A normality test (D'Agostino-Pearson) was performed on all experimental data to assess the data distribution, which did not have a normal distribution in all cases. Data analysis was performed using a non-parametric Kruskal–Wallis test and Dunn's multiple comparison tests to analyze significant differences between groups. Statistical analyses were carried out using GraphPad Prism (v 8.0.2). The significance threshold was set at 5 % ($*p < 0.05$) and 1 % ($**p < 0.01$). All data are represented as box plots with median, minimum, and maximum with min, max, and mean indicated with "+" symbol using GraphPad Prism (v 8.0.2).

3. Results and discussion

3.1. Characterization of MEW structures

3.1.1. Structural and morphological characterization

The MEW printing technique enables the high-fidelity printing of thermoplastic polymers. The cartridge is heated, and air pressure is applied to the cartridge's piston to extrude the material through a stainless-steel needle. A potential difference between the needle and the

printing bed is applied to attract the filament and obtain a well-defined pattern, as shown in Fig. 1a. In this work, the MEW printing process was used to fabricate a fibrous structure made of PCL with different pore designs and sizes. Two patterns were investigated: a square pore size geometry, named GRID, consisting of alternating layers with vertical (0°) and horizontal (90°) fibers, and a hexagonal pore shape geometry, named HEX, with honeycomb pores (Fig. 1b). Both patterns were fabricated with three different pore sizes: 0.6, 0.8, and 1.0 mm. The pore size of GRID structures was set as the distance between two consecutive fibers, while for HEX structures, it was determined as the radius of the circumscribed circle of the hexagon, as illustrated in Fig. 1b and Fig. S1. The calculated porosities of the MEW structures are reported in Table 1. Representative images of GRID and HEX structures varying in pore size are shown in Fig. 1c. The average PCL fiber width was equal to 11.4 ± 0.4 μm. Thanks to the spatial precision of the MEW printing technique, PCL fibers were aligned at the intersection points of the structures in both designs, as illustrated in the SEM images of Fig. 1d.

3.1.2. Mechanical characterization

The mechanical properties of the MEW structures were characterized using uniaxial compression and tensile testing (Fig. 2). For compression tests, MEW structures were punched with a biopsy puncher (diameter = 5 mm) and two punched structures were stacked on top of each other to perform the compression tests (Fig. 2a and b). There was a non-significant trend towards a decrease in the compression modulus for higher pore sizes for the GRID structure (from 20.6 ± 7.4 kPa for the 0.6 mm to 11.1 ± 4.6 kPa for the 1.0 mm) (Fig. 2c). This observation is consistent with previous studies that printed MEW structures with different pore sizes [12]. In contrast, the compression properties of the HEX structures were 17.14 ± 2.14 kPa, 12.35 ± 3.95 kPa, and 18.22 ± 5.37 kPa for the pore size at 0.6 mm, 0.8 mm, and 1.0 mm, respectively.

Table 1
Porosities of MEW structures based on their pore shape and size.

Pore shape	Pore size	Porosity
GRID/HEX	1.0 mm	97.73 %
GRID/HEX	0.8 mm	97.17 %
GRID/HEX	0.6 mm	96.23 %

Tensile tests were also performed by clamping rectangular-shaped MEW structures (25 x 10 × 1 mm). We found that the pore shape and size significantly influenced the tensile modulus of the fibrous structures (Fig. 2e and f). A significant reduction was observed between the 0.6 mm and 1.0 mm pore sizes for the GRID structures (from 196.3 ± 18.2 kPa to 84.5 ± 14.8 kPa) and between all HEX-shaped structures (from 553 ± 36.3 kPa to 279.9 ± 47.9 kPa). HEX structures generally displayed significantly greater tensile modulus than GRID structures printed at the same pore size.

Polyesters have the drawback of limited elastic deformation, and the scaffold deformation can be improved by setting specific geometric patterns. Honeycomb (e.g., HEX shape) is a common microstructure used for several applications (e.g., cardiac stents) having a deformation up to 40 % [43]. Our results showed a remarkable deformation, reaching values higher than 400 % for all cases (Fig. 2e). Furthermore, the design of the structures had a significant impact on their tensile modulus since the hexagon shape is demonstrated to have a low percentage of energy reduction with respect to other shapes (isosceles/right-angle triangle, square, isosceles/right-hand trapezium) due to the high structural deformation till break [44]. Generally, a smaller pore size implied a stiffening of the structure, with HEX structures exhibiting higher values

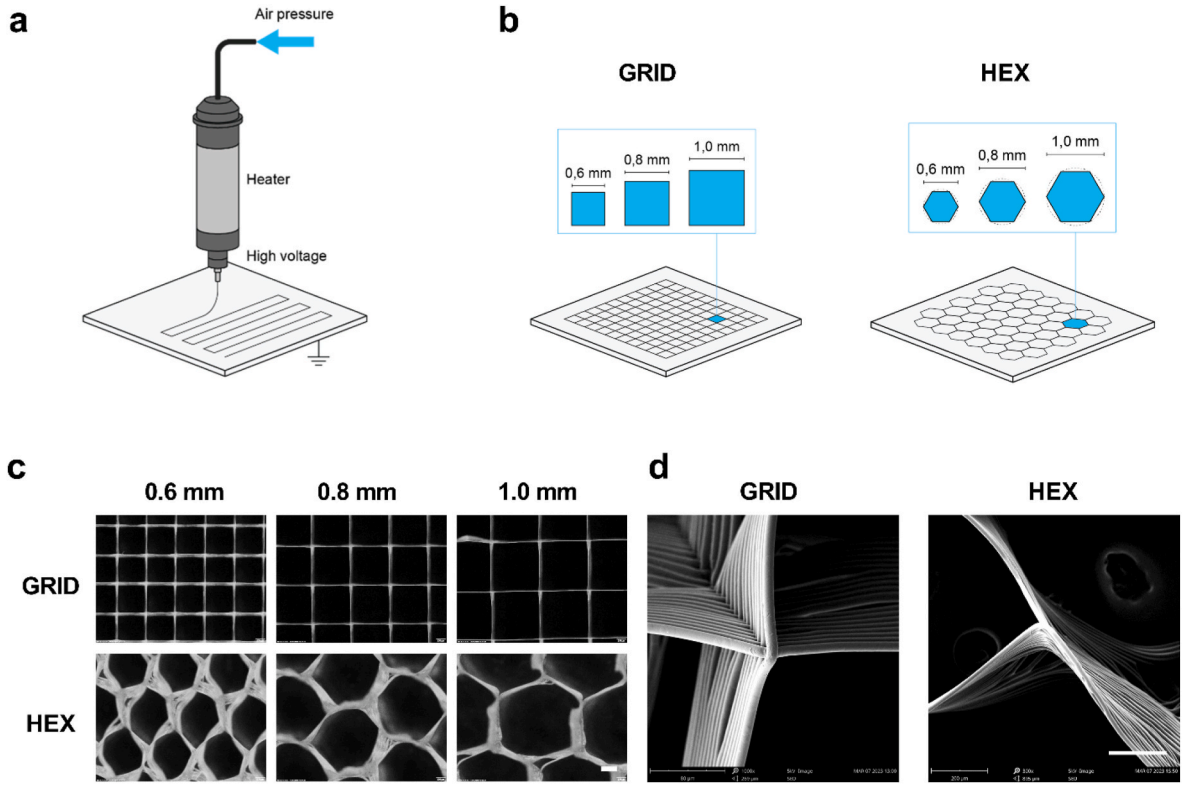

Fig. 1. The MEW printing technique for fabricating fibrous structures with square and hexagon-shaped pore designs. a) Depiction of the printing process through the MEW technique: air pressure is applied to the cartridge's piston to flow out the melted polymer by a heated cartridge; a high voltage is applied between the needle and the printing bed to precisely depose the material. b) Depiction of the targeted MEW patterns: GRID (left) and HEX (right). The zoomed boxes highlight the pore sizes considered in this study. c) Inverted microscope images of MEW structure made by precisely depositing melted PCL to visualize the variation in terms of pore shape (GRID and HEX) and pore size (0.6 mm, 0.8 mm, and 1.0 mm); scale bar = 400 μm. d) SEM images of the intersection points of the MEW structures having a GRID (left) and HEX (right) pattern; scale bar = 200 μm.

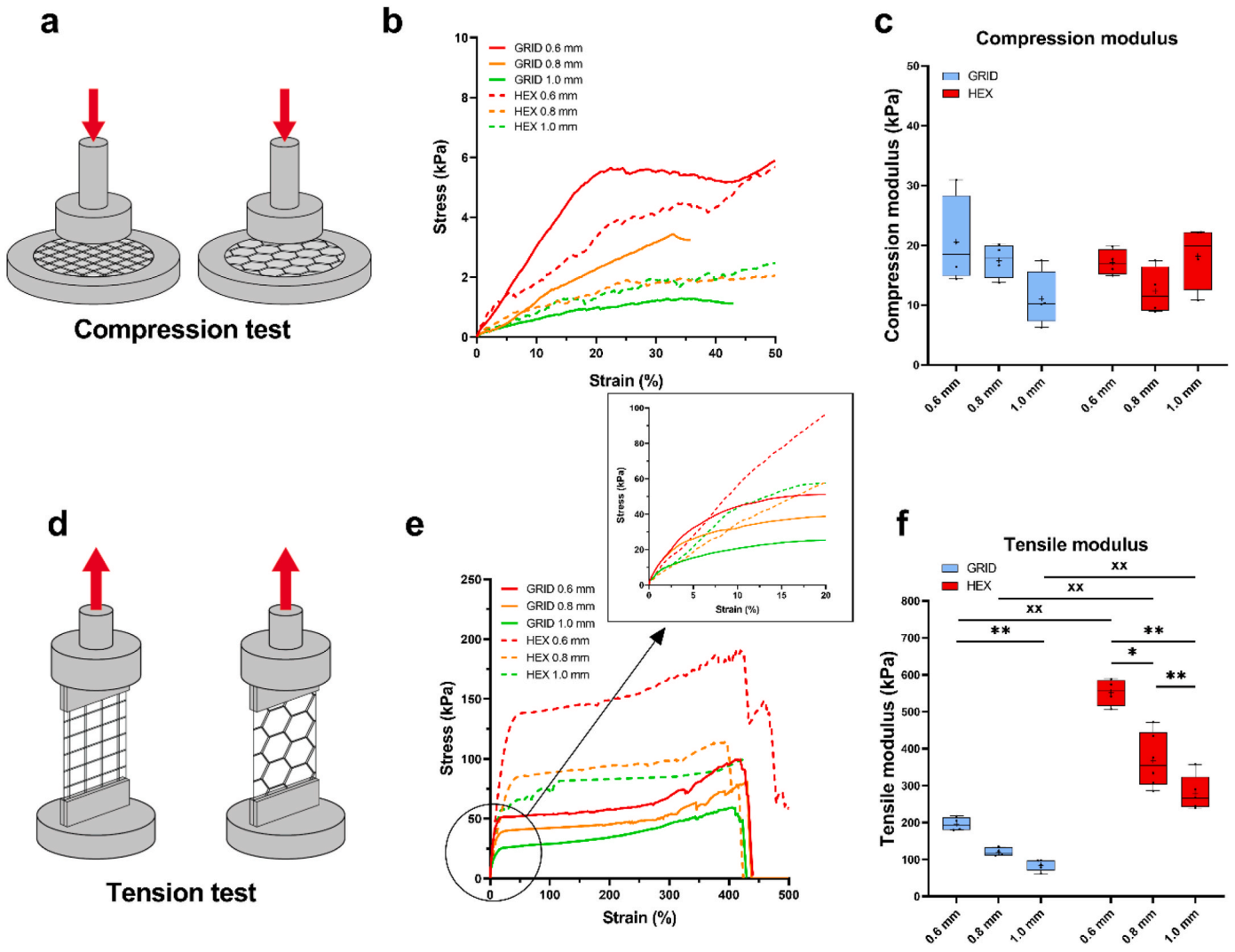

Fig. 2. Mechanical characterization of MEW structures. a) Depiction of the compression test performed on punched MEW structures. b) Stress-strain curves recorded during the compression test and c) the compression modulus of MEW structure varying the pore shape (GRID, light blue - HEX, red) and the pore size (0.6 mm, 0.8 mm, and 1.0 mm). d) Depiction of tension test carried out on cut rectangular MEW structures. e) Stress-strain curves recorded during the tension test with the zoomed box showing the curves at strain up to 20 %. f) Tensile modulus of the previous MEW structure varying the pore shape size. Legend: */** = differences between pore size; $^{X}/^{XX}$ = differences between pore shape; $^{*}/^{X}$ $p < 0.05$; $^{**}/^{XX}$ $p < 0.01$.

at each pore size than GRID structures. These findings are in contrast to previous literature, which reported lower modulus values for HEX-shaped structures compared to GRID ones, even when the pore shape was rectangular [36]. The HEX-shaped structures were printed by employing trapezoidal velocity profiles, which effectively doubled the transitional speed compared to that used for printing GRID structures. As a result, wider filaments were generated, enabling the successful creation of the desired shapes but also producing stiffer structures.

3.2. Evaluation of hydrogel injection forces varying MEW structure pore shape and size

As shown in Fig. S4a, the flow curves of the A3G3 hydrogel solution showed a consistent shear-thinning behavior, suggesting its suitability as an injectable material. Rheological indexes were extracted by flow curves of the A3G3 hydrogel solution and reported in Table S1 n was equal to 0.64 ± 0.02, and K was equal to 2.58 ± 0.38 Pa·s^{n}.

The injection forces were measured during the extrusion of MEW structures embedded in the A3G3 hydrogel solution. As depicted in Fig. 3a, the MEW structure was loaded within 2.5 mL of the A3G3 hydrogel solution inside a 6 mL cartridge. The cartridge was placed vertically through custom support to let the material flow vertically through a displacement-controlled test, recording the injection force with a 10 N load cell. The MEW structure was stretched while flowing through the needle, which had a smaller diameter than the punched structure. After injection, they returned to their original shape.

The injection forces required to extrude the hydrogel embedding MEW structures designed with both GRID and HEX pore shapes with three different pore sizes (0.6, 0.8 and 1.0 mm) through three different stainless-steel needles (18G, 16G, and 14G) were then measured (Fig. 3b). The injection forces were calculated as the difference between the maximum peak force (Fig. S2) during MEW structure extrusion and the force required to extrude the unreinforced A3G3 hydrogel solution. We found that the pore size significantly affected the injection forces, with statistically significant differences observed for both patterns. HEX structures generally require higher injection forces than GRID structures, which can be linked to differences in the tensile moduli of both network types (Fig. 2f). This suggests that structures with higher tensile modulus may provide higher resistance to deforming during the extrusion phase. The HEX-shaped grid showed a lower stretchability, leading to occlusion of the needle in the case of a smaller needle diameter (e.g., 18 G). Furthermore, injection forces decreased when larger needle

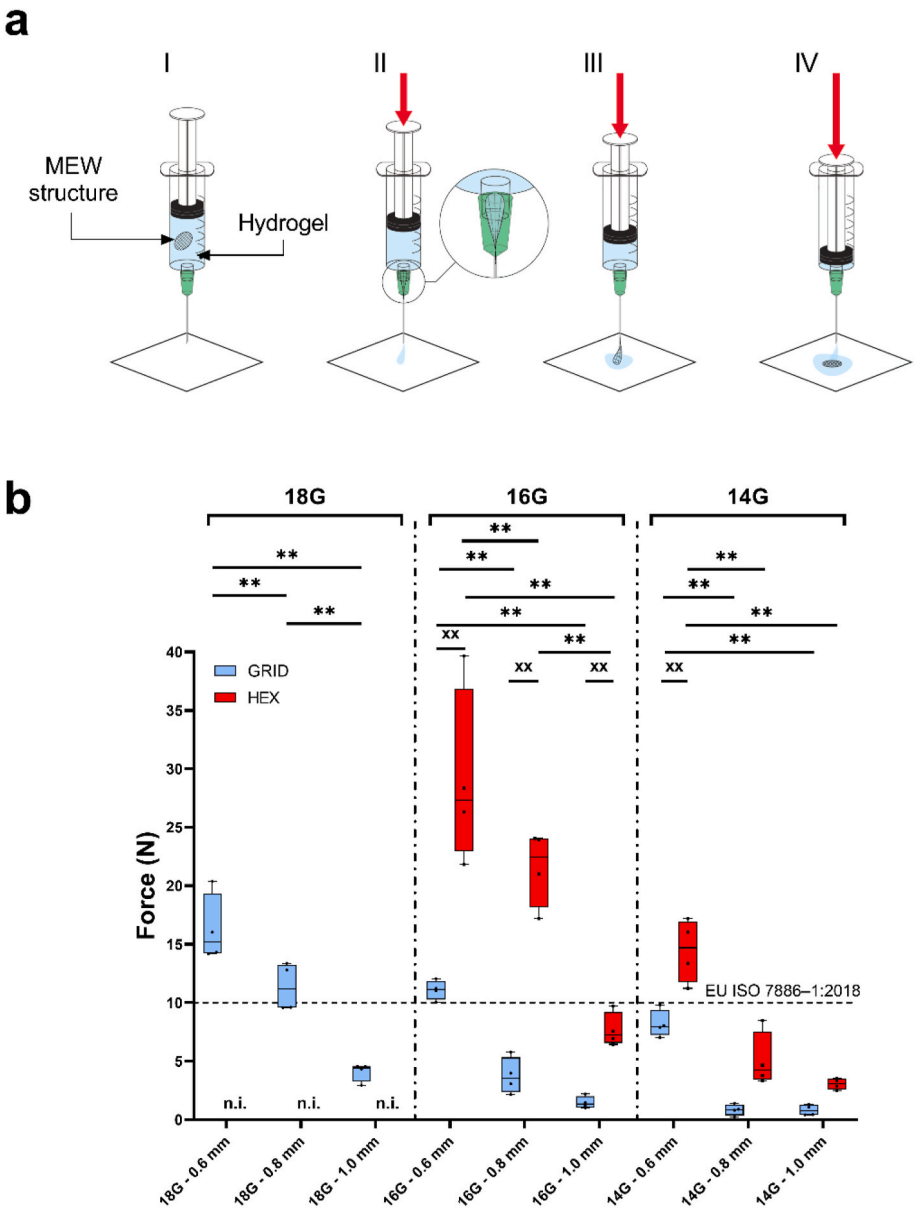

Fig. 3. Evaluation of the hydrogel injection forces varying MEW structure pore shape and size. a) Depiction of the injection steps in which a MEW structure is flowed out through a stainless-steel needle. The MEW structure is stretched while the material is extruded and, after injection, it returns to the original shape. b) Injection forces recorded to flow the MEW structures-laden hydrogel solution by 18G, 16G, and 14G stainless-steel needles. MEW structures with GRID and HEX pore shapes and different pore sizes (0.6 mm, 0.8 mm, and 1.0 mm) were analyzed for each needle size. Legend: n.i. = not injectable; */** = differences between pore size; $^{X}/^{XX}$ = differences between pore shape; $^{*}/^{X}$ $p < 0.05$; $^{**}/^{XX}$ $p < 0.01$.

diameters were analyzed (Fig. 3b).

It is worth mentioning that no data on injection forces for MEW structures dispersed in hydrogel formulations are available in the literature. Castilho et al. [36] proposed the delivery of a PCL-based MEW printed sheet (4 cm × 1 cm × 1 mm) through a catheter-like tubing (diameter = 1.5 mm) onto a beating porcine heart for myocardial tissue treatment. Here, the viability of cells embedded in the reinforced hydrogels with a MEW printed sheet remained intact after injection. Nonetheless, injection forces were not reported. Also, cell viability was not analyzed in the long-term (only for the first two days). In addition, Molas et al. [45] showed that a 4 cm^2 mesh of PCL/gelatin core-shell nanofibers produced by electrospinning can be injected through a 1.55 mm catheter. Even though the viability of human mesenchymal stem cells seeded on the mesh was close to 80 % after injection, they included SEM images of a change in the fiber distribution after injection (from random to more aligned). Finally, Wang and colleagues produced and injected a PCL-based ultra-flexible conductive scaffold (with just one layer) via MEW with a nanolayer of gold via sputter coating to repair peripheral nerve defects [37]. Our results show for the first time a precise measuring of injection forces produced by the extrusion of a MEW structure printed by varying two patterns and three pore sizes after being immersed into an injectable hydrogel.

The EU ISO 7886–1:2018 standard suggests a clinically acceptable injection force of less than 10 N. The MEW structure with a GRID-shaped design and a pore size of 1.0 mm was successfully injected with an 18G stainless-steel needle using a force of 4.09 ± 0.77 N (Fig. 3b, left). The GRID-shaped structures with pore sizes of 0.8 mm and 1.0 mm were injected through 16G needles with injection forces of 3.74 ± 1.55 N and 1.46 ± 0.52 N, respectively. Only the HEX-shaped structure with a pore size of 1.0 mm required an injection force within the 10 N threshold (7.67 ± 1.45 N) close to the ISO limit (Fig. 3b, center) when injected through a 14G needle. All MEW-printed structures could be injected

using 14G needles (Fig. 3b, right). The GRID-shaped structures with pore sizes from 0.6 mm to 1.0 mm required injection forces of 8.19 ± 1.17 N, 0.83 ± 0.48 N, and 0.80 ± 0.45 N, respectively, when injected with 14G needles (Fig. 3b, right). The HEX-shaped structures required injection forces of 14.35 ± 2.87 N, 5.05 ± 2.35 N, and 3.06 ± 0.47 N, respectively, for 0.6 mm, 0.8 mm, and 1.0 mm pore sizes. Therefore, the lowest injection force of 0.80 ± 0.45 N was recorded for the GRID structure with a 1.0 mm pore size when injected with a 14G needle. Even though the HEX-shaped structure with 0.6 mm of pore size had an injection force higher than 10 N, all configurations extruded using 14G needles were then selected for subsequent tests to compare the resulting mechanical properties upon cross-linking, as reported in the next sections.

Following injection, the MEW structures returned to their original shape. As proof, they were thoroughly rinsed with deionized water to remove the uncross-linked hydrogel solution and then dried for examination using a microscope. Fig. S3 displays representative images of the

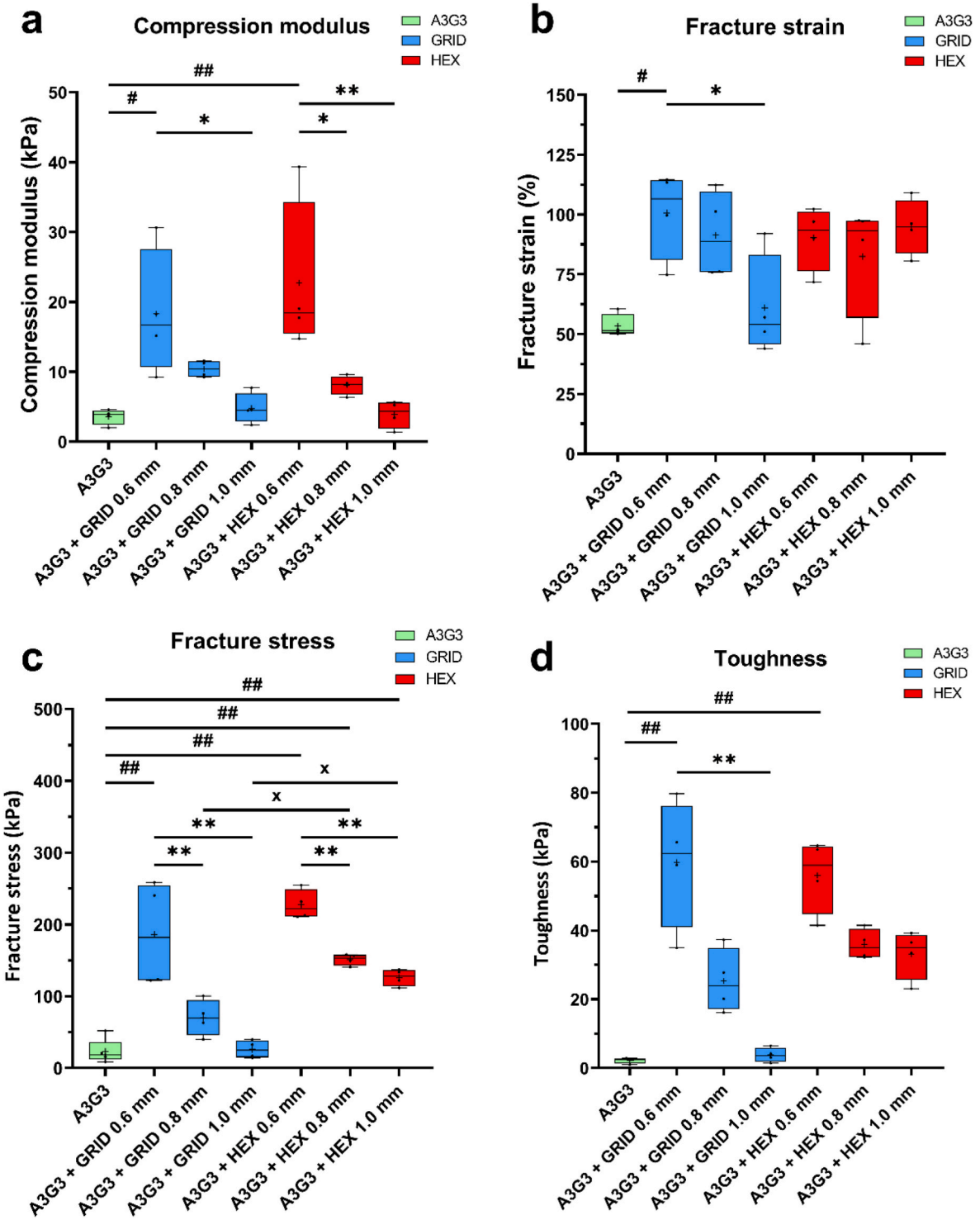

Fig. 4. Mechanical characterization of unreinforced (A3G3) cross-linked hydrogel and MEW-reinforced cross-linked hydrogels after injection (14G) and cross-linking in terms of a) compression modulus, b) fracture strain, c) fracture stress, and d) toughness. Legend: */** = differences between pore sizes; $^{X}/^{XX}$ = differences between pore shape; $^{\#}/^{\#\#}$ = differences with the control (A3G3) */^{X}/$^{\#}$p < 0.05; **/^{XX}/$^{\#\#}$p < 0.01.

MEW structures before and after injection. The original shape of the structures (before injection) is shown in Fig. S3a. When injected using an 18G needle, a minor distortion was observed in the GRID-shaped structures with pore sizes of 1.0 mm and 0.8 mm, and some filaments were disrupted within the GRID structure with a pore size of 0.6 mm (Fig. S3b). Nevertheless, it was evident that the injection process did not impact the structure or pore shape of both GRID- and HEX-shaped structures when injected through 16G (Fig. S3c) and 14G (Fig. S3d) needles. These findings demonstrate that MEW structures embedded in a hydrogel solution can be successfully injected without causing any permeant structural damage.

3.3. Mechanical characterization of hydrogels reinforced by MEW structures

The reinforced hydrogel solutions, incorporating various MEW structure configurations, were delivered into a cylindrical mold using 14G needles and cross-linked with a $CaCl_2$ solution for 10 min to evaluate the mechanical reinforcement provided by the MEW structures. We compared all configurations, even the one integrating the HEX structure with 0.6 mm of pore size, which resulted in an injection force higher than 10 N (Figs. 2c and 3b, left).

All MEW-reinforced cross-linked hydrogels exhibited a superior compression modulus compared to the unreinforced counterpart (named A3G3). Such results indicate that the embodiment of the MEW structure, independently from the geometrical parameters analyzed, effectively reinforced the hydrogels (Fig. 4a). More in detail, both MEW structures with a pore size of 0.6 mm showed statistically significant differences compared to the not-reinforced hydrogel (3.58 ± 1.12 kPa) with values equal to 18.31 ± 9.03 kPa (5.1-fold) and 22.72 ± 11.23 kPa (6.3-fold), respectively for GRID and HEX pore shapes. Moreover, the cross-linked hydrogel reinforced with the GRID structure with 0.6 mm pore size exhibited statistically significant differences with the same structure with the lowest pore size (1.0 mm) equal to 4.76 ± 2.20 kPa. On the other hand, the HEX-shaped structure with pores of 0.6 mm showed statistically significant differences compared to both reinforcements at 0.8 mm ($^{*}p < 0.05$, 8.09 ± 1.37 kPa) and 1.0 mm ($^{**}p < 0.01$, 3.91 ± 1.97 kPa). The MEW structures significantly enhanced the cross-linked hydrogels' mechanical properties, with compression moduli closely approaching those of the MEW templates themselves (Fig. 2c), particularly in the case of the 0.6 mm pore size. This level of reinforcement is comparable to results reported by Visser et al. [12], who used a GRID-shaped MEW structure to reinforce an alginate-based hydrogel with similar pore sizes.

Castilho et al. [23] reported similar results, achieving a compression modulus of 26 ± 3 kPa (1.7-fold increase) by filling a GRID structure with a 0.8 mm pore size with gelatin methacryloyl (GelMA) hydrogel (compression modulus of 15 ± 3 kPa), targeting the middle and deep zones of articular cartilage. Xu et al. [46] made significant strides in tissue-engineered heart valves by combining tri-layered GRID structures with GelMA-based hydrogels, achieving compression moduli of 8 and 9 kPa (increases of 4- and 4.5-fold) with 0.6 and 1.0 mm pore sizes, respectively. Ruijter et al. [47] explored composite constructs generated by infusing MEW fiber structures with hydrogels, showing a remarkable 4.5-fold increase in the compression equilibrium modulus from 11.90 ± 4.09 kPa (printing, gel alone) to 53.02 ± 8.73 kPa (converged printing, reinforced gel), and a 3.8-fold increase from 17.02 ± 6.79 kPa (cast, gel alone) to 64.17 ± 13.41 kPa (cast, reinforced gel). Galarraga et al. [48] demonstrated that composites fabricated with MEW structures of 0.4 mm spacing could increase the moduli of soft NorHA hydrogels by ~50-fold, although only the GRID structure with a pore size of 0.8 mm can be directly compared to our work, which showed a compression modulus of ~50 kPa (a ~25-fold increase). Dubay et al. [28] highlighted the tunability of fiber-reinforced hydrogels by incorporating highly porous PCL fibrous meshes into GelMA hydrogel, achieving a compression modulus ranging from ~70 kPa to ~300 kPa (~4.2-fold increase), demonstrating the significant enhancement possible by increasing the number of fibrous meshes. Bas et al. [49] explored the reinforcement of fibrin and sPEG/Hep hydrogels using fibrous networks with pore sizes of 0.6 mm, 0.4 mm, and 0.2 mm. They reported a compression modulus of 43.0 ± 6.2 kPa for the 0.6 mm pore size network, with a 4-fold increase in fibrin and a 14-fold increase in sPEG/Hep hydrogels, suggesting a synergistic interaction between the fibrous network and hydrogel matrix. In a related study, Bas et al. [50] produced fiber-reinforced GelMA/HAMA composites, showing a compression modulus of 448.2 ± 97.8 kPa (~10-fold increase) for a 0.8 mm pore size network, though these values are not directly comparable to our findings. Größbacher et al. [51] utilized volumetric bioprinting combined with MEW to create a tubular hydrogel-based composite for vascular applications, with a reinforced compression modulus of 20.3 ± 3.2 kPa (3.9-fold increase), in line with previous studies and similar to our results. Diloksumpan et al. [17] used MEW to fabricate osteochondral plugs with spatially organized polymeric microfibers, achieving a ~20-fold increase in compression modulus from ~10 kPa (GelMA alone) to ~200 kPa with a 0.3 mm pore size, though this technique is not suitable for minimally invasive procedures like ours. Interestingly, other studies from the same research groups have reported significant increases in fiber-reinforced hydrogels with larger pore sizes, comparable to ours. Castilho et al. [16] reported a compression modulus of 81.4 ± 10.3 kPa (~19-fold increase) and 122.2 ± 16.21 kPa (~29-fold increase) for composites with 0.8 mm and 0.6 mm pore sizes, respectively, using GRID-pore designs. These significant increments are notably different from other literature findings. The stiffness of the fiber component usually contributes the most to the composite stiffness and initially increases with its volumetric fraction [9]. However, here reinforcement behavior may significantly vary depending on the specific materials of the hydrogel, their volumetric fraction, and stiffness, beyond the pore shape and size of the MEW structure used.

From the measurement of the fracture strain values, no relevant differences were observed in most of the samples (Fig. 4b). There were statistically significant differences between the reinforced cross-linked hydrogel using a GRID structure with a pore size of 0.6 mm and the unreinforced cross-linked hydrogel ($^{\#}p < 0.05$) and the GRID-shaped structure with the lowest pore size ($^{*}p < 0.05$). However, the unreinforced cross-linked hydrogel had a fracture strain of 53.38 ± 4.78 %, while the other configurations ranged between a minimum of 61.01 ± 21.34 % (GRID with 1.0 mm) and a maximum of 98.60 ± 18.50 % (GRID with 0.6 mm).

The fracture stress values decreased with increasing the pore size in both GRID and HEX structures (Fig. 4c), as the compression moduli (Fig. 4a). The unreinforced cross-linked hydrogel showed a fracture stress of 23.09 ± 16.74 kPa significantly different concerning the MEW structures with GRID shape and pore size of 0.6 mm and with HEX shape and each pore size. Moreover, both shapes with 0.6 mm showed the highest fracture stress values (186.2 ± 73.45 kPa and 227.4 ± 20.56 kPa, respectively for GRID and HEX) with statistically significant differences with respect to their other configurations with wider pore sizes ($^{**}p < 0.01$). Unfortunately, no works reported fracture strain or stress values to be compared with our findings.

Regarding toughness, the measurement of the amount of energy that can be absorbed through mechanisms (i.e., plastic deformation) before a fracture occurs, it is evident that the structures with higher energy dissipation were the GRID- and the HEX-shaped structures with a pore size of 0.6 mm equal to 59.8 ± 18.71 kPa and 55.98 ± 10.72 kPa, respectively. Indeed, they were statistically significantly different from the toughness value of the control (A3G3, 2.180 ± 0.84 kPa). However, no other differences were evidenced in Fig. 4d. As shown, the MEW structure with the tightest pore size and those with HEX-shaped pores allowed the cross-linked hydrogel to absorb more energy before reaching the breakpoint, which can be beneficial for load-bearing applications, such as articular cartilage [52]. These structures had the ability to resist the growth of defects into propagating cracks, higher than

structures with wider pore size but independently by the pore shape [9,53].

3.4. Influence of different hydrogels

In addition to the A3G3 hydrogel solution, we included two other hydrogels in our analysis: VG-RGD and GGMA [42,54,55]. First, we characterized the materials in terms of rheological properties, by evaluating their viscosity, as it strongly influences the injection force [56]. The flow curves of the hydrogel solutions demonstrated a consistent shear-thinning trend, indicating good injectability potential. Notably, GGMA exhibited the highest viscosity, while VG-RGD displayed the lowest viscosity across the entire range of shear rates, as shown in Fig. S4a. These findings were further confirmed by evaluating the rheological indexes, n and K, reported in Table S1, with the GGMA solution showing a statistically significant higher viscosity than the other two hydrogels. These values are in line with previous literature findings on these hydrogel types [54].

We tested the GRID structure with a 1.0 mm pore size, which had shown the lowest injection force during the previous screening within the A3G3 hydrogel solution, with the VG-RGD and GGMA hydrogel solutions. During the injection step, no significant differences were observed in the flow of MEW structures within VG-RGD and GGMA solutions compared to the A3G3 solution (0.80 ± 0.45 N) (Fig. S4b). The extrusion of reinforced VG-RGD and GGMA hydrogel solutions required injection forces of 1.40 ± 0.25 N and 0.81 ± 0.24 N, respectively. This suggests that the injection forces reported in both Fig. 3b and Fig. S4b primarily depended on the MEW structure itself rather than the viscosity of the hydrogels. Even though the K index of GGMA was statistically higher than the others, VG-RGD showed slightly less viscosity than the A3G3 hydrogel solution (Table S1).

The reinforced VG-RGD and GGMA hydrogel solutions were delivered via 14G needles into a cylindrical mold and cross-linked to verify the reinforcement provided by the presence of the MEW structure (GRID with 1.0 mm pore size) in terms of compressive modulus. The MEW-reinforced cross-linked hydrogels exhibited superior compressive moduli compared to their unreinforced counterparts, indicating effective reinforcement by the MEW structure. Specifically, the MEW-reinforced A3G3 and VG-RGD hydrogels resulted in 1.33- and 1.57-fold increases, respectively, over their unreinforced versions, while the reinforced GGMA showed a 3.01-fold increase compared to the unreinforced GGMA (Fig. S4c). These results highlight the vital role of MEW templates in reinforcing natural hydrogels.

The reinforcement effect was influenced not solely by the pore shape and size of the MEW structure, which remained constant across all cases, but also by the inherent characteristics of the hydrogel [12,50]. The most pronounced difference between unreinforced and reinforced cross-linked hydrogels occurred with GGMA, which was photo-crosslinked using visible light. This result is likely due to the covalent bonds formed between the photo-crosslinked hydrogel and the MEW structure, which are stronger than the ionic bonds formed in the other two hydrogels. Our findings align with those of Moo et al. [57], who demonstrated that MEW structures specifically enhance fluid pressurization in GelMA hydrogels, but not in agarose or alginate. Their study concluded that covalently cross-linked hydrogels, such as GelMA, can effectively bond with MEW structures, increasing fluid pressure resistance during compressive loading.

In conclusion, our study demonstrates for the first time the possibility of injecting different hydrogel solutions reinforced by MEW structures to be cross-linked *in situ*, resulting in superior mechanical properties compared to their unreinforced counterparts. This confirms the potential of MEW structures to effectively reinforce various classes of hydrogels, as previously shown with non-injected hydrogels and MEW structures [9,48].

4. Conclusions

In this work, melt electro-writing (MEW) was utilized to fabricate fibrous networks using GMP-grade polycaprolactone, a synthetic polymer widely used in tissue engineering. MEW structures with various pore shapes (square and hexagonal) and sizes (0.6, 0.8, and 1.0 mm) were produced to investigate their influence on injectability and mechanical properties. This technique allowed for the precise deposition of fibers having a diameter of 11.4 ± 0.4 μm. MEW structures with hexagonal pores exhibited a significantly higher tensile modulus than the ones with square pores, although no differences were observed in the compression moduli. The fibrous structures were embedded into an alginate-gelatin-based hydrogel solution and injected through stainless steel needles of different diameters (18G, 16G, and 14G), compatible with clinical applications. The hexagonal-shaped structures could not be injected using the thinnest needles (18G) and, for larger needles (16G and 14G), they required higher injection forces than square-shaped structures, at equivalent pore sizes. Larger pore sizes implied smaller injection forces. Only a few conditions were compatible with the limits defined by the EU ISO 7886–1:2018 standard. Notably, during injection, the MEW structures experienced stretching inside the needles but quickly returned to their original shape without significant damage. Our results quantify, for the first time, the force needed to inject a hydrogel solution reinforced with MEW structures of varying pore shapes and sizes, clarifying the role of these parameters on the injection force. Hydrogel reinforcement also resulted depending on the pore shape and size of the MEW structures. Integrating MEW structures with a 0.6 mm pore size in the cross-linked hydrogel resulted in a compression modulus increase of up to 6.34-fold compared to the unreinforced cross-linked counterpart.

CRediT authorship contribution statement

Diego Trucco: Conceptualization, Formal analysis, Data curation, Writing – original draft. **Rory Gibney:** Methodology, Writing – review & editing. **Lorenzo Vannozzi:** Methodology, Validation, Writing – review & editing. **Gina Lisignoli:** Validation, Supervision, Writing – review & editing. **Daniel J. Kelly:** Methodology, Validation, Supervision, Writing – review & editing. **Leonardo Ricotti:** Conceptualization, Validation, Supervision, Funding acquisition, Writing – review & editing.

Declaration of competing interest

The authors declare that they have no known competing financial interests or personal relationships that could have appeared to influence the work reported in this paper.

Acknowledgment

This work received both financial and technical support from INAIL, in the framework of the project MioPRO^2 (*Engineered patient-specific muscles for the restoration of myoelectric channels and prosthesis control*), grant agreement No PR23-CR-P1, and from the European Union's Horizon 2020 research and innovation program, grant agreement No 814413, project ADMAIORA (*ADvanced nanocomposite MAterIals fOr in situ treatment and ultRAsound-mediated management of osteoarthritis*). The authors acknowledge the contribution of Mr. Giovanni Gonnella and Mr. Matthia Bonizzi for their technical support in the activities carried out at Trinity College of Dublin.

Appendix A. Supplementary data

Supplementary data to this article can be found online at https://doi.org/10.1016/j.jmrt.2025.03.133.

References

[1] Alonso JM, Andrade del Olmo J, Perez Gonzalez R, Saez-Martinez V. Injectable hydrogels: from laboratory to industrialization. Polymers 2021;13(4):650.
[2] Gaharwar AK, Singh I, Khademhosseini A. Engineered biomaterials for in situ tissue regeneration. Nat Rev Mater 2020;5(9):686–705.
[3] Mandal A, Clegg JR, Anselmo AC, Mitragotri S. Hydrogels in the clinic. Bioengineering & Translational Medicine 2020;5(2):e10158.
[4] O'Brien S, Brannigan RP, Ibanez R, Wu B, O'Dwyer J, O'Brien FJ, Cryan S-A, Heise A. Biocompatible polypeptide-based interpenetrating network (IPN) hydrogels with enhanced mechanical properties. J Mater Chem B 2020;8(34):7785–91.
[5] Qiu Y, Park K. Superporous IPN hydrogels having enhanced mechanical properties. AAPS PharmSciTech 2003;4(4):51.
[6] Affatato S, Trucco D, Taddei P, Vannozzi L, Ricotti L, Nessim GD, Lisignoli G. Wear behavior characterization of hydrogels constructs for cartilage tissue replacement. Materials 2021;14(2):428.
[7] Sakr MA, Sakthivel K, Hossain T, Shin SR, Siddiqua S, Kim J, Kim K. Recent trends in gelatin methacryloyl nanocomposite hydrogels for tissue engineering. J Biomed Mater Res 2022;110(3):708–24.
[8] Xing W, Tang Y. On mechanical properties of nanocomposite hydrogels: searching for superior properties. Nano Materials Science 2022;4(2):83–96.
[9] Beckett LE, Lewis JT, Tonge TK, Korley LTJ. Enhancement of the mechanical properties of hydrogels with continuous fibrous reinforcement. ACS Biomater Sci Eng 2020;6(10):5453–73.
[10] Ji D, Kim J. Recent strategies for strengthening and stiffening tough hydrogels. Advanced NanoBiomed Research 2021;1(8):2100026.
[11] Trucco D, Vannozzi L, Teblum E, Telkhozhayeva M, Nessim GD, Affatato S, Al-Haddad H, Lisignoli G, Ricotti L. Graphene oxide-doped gellan gum–PEGDA bilayered hydrogel mimicking the mechanical and lubrication properties of articular cartilage. Advanced Healthcare Materials n/a 2021;(n/a):2001434.
[12] Visser J, Melchels FPW, Jeon JE, van Bussel EM, Kimpton LS, Byrne HM, Dhert WJA, Dalton PD, Hutmacher DW, Malda J. Reinforcement of hydrogels using three-dimensionally printed microfibres. Nat Commun 2015;6(1):6933.
[13] Brown TD, Dalton PD, Hutmacher DW. Direct writing by way of melt electrospinning. Advanced materials (Deerfield Beach, Fla.) 2011;23(47):5651–7.
[14] Hochleitner G, Jüngst T, Brown TD, Hahn K, Moseke C, Jakob F, Dalton PD, Groll J. Additive manufacturing of scaffolds with sub-micron filaments via melt electrospinning writing. Biofabrication 2015;7(3):035002.
[15] Wunner FM, Bas O, Saidy NT, Dalton PD, Pardo EMD, Hutmacher DW. Melt electrospinning writing of three-dimensional poly(ε-caprolactone) scaffolds with controllable morphologies for tissue engineering applications. J Vis Exp 2017;130.
[16] Castilho M, Hochleitner G, Wilson W, van Rietbergen B, Dalton PD, Groll J, Malda J, Ito K. Mechanical behavior of a soft hydrogel reinforced with three-dimensional printed microfibre scaffolds. Sci Rep 2018;8(1):1245.
[17] Diloksumpan P, de Ruijter M, Castilho M, Gbureck U, Vermonden T, van Weeren PR, Malda J, Levato R. Combining multi-scale 3D printing technologies to engineer reinforced hydrogel-ceramic interfaces. Biofabrication 2020;12(2):025014.
[18] Eichholz KF, Gonçalves I, Barceló X, Federici AS, Hoey DA, Kelly DJ. How to design, develop and build a fully-integrated melt electrowriting 3D printer. Addit Manuf 2022;58:102998.
[19] Eichholz KF, Hoey DA. Mediating human stem cell behaviour via defined fibrous architectures by melt electrospinning writing. Acta Biomater 2018;75:140–51.
[20] Eichholz KF, Freeman FE, Pitacco P, Nulty J, Ahern D, Burdis R, Browe DC, Garcia O, Hoey DA, Kelly DJ. Scaffold microarchitecture regulates angiogenesis and the regeneration of large bone defects. Biofabrication 2022;14(4):045013.
[21] Barceló X, Eichholz KF, Gonçalves IF, Garcia O, Kelly DJ. Bioprinting of structurally organized meniscal tissue within anisotropic melt electrowritten scaffolds. Acta Biomater 2023;158:216–27.
[22] Afghah F, Iyison NB, Nadernezhad A, Midi A, Sen O, Saner Okan B, Culha M, Koc B. 3D fiber reinforced hydrogel scaffolds by melt electrowriting and gel casting as a hybrid design for wound healing. Adv Healthcare Mater 2022;11(11):2102068.
[23] Castilho M, Mouser V, Chen M, Malda J, Ito K. Bi-layered micro-fibre reinforced hydrogels for articular cartilage regeneration. Acta Biomater 2019;95:297–306.
[24] Dwivedi R, Kumar S, Pandey R, Mahajan A, Nandana D, Katti DS, Mehrotra D. Polycaprolactone as biomaterial for bone scaffolds: review of literature. Journal of Oral Biology and Craniofacial Research 2020;10(1):381–8.
[25] Woodruff MA, Hutmacher DW. The return of a forgotten polymer—polycaprolactone in the 21st century. Prog Polym Sci 2010;35(10):1217–56.
[26] Eichholz KF, Von Euw S, Burdis R, Kelly DJ, Hoey DA. Development of a new bone-mimetic surface treatment platform: nanoneedle hydroxyapatite (nnHA) coating. Adv Healthcare Mater 2020;9(24):2001102.
[27] Arif ZU, Khalid MY, Noroozi R, Sadeghianmaryan A, Jalalvand M, Hossain M. Recent advances in 3D-printed polylactide and polycaprolactone-based biomaterials for tissue engineering applications. Int J Biol Macromol 2022;218:930–68.
[28] Dubey N, Ferreira JA, Daghrery A, Aytac Z, Malda J, Bhaduri SB, Bottino MC. Highly tunable bioactive fiber-reinforced hydrogel for guided bone regeneration. Acta Biomater 2020;113:164–76.
[29] Qiao Z, Lian M, Han Y, Sun B, Zhang X, Jiang W, Li H, Hao Y, Dai K. Bioinspired stratified electrowritten fiber-reinforced hydrogel constructs with layer-specific induction capacity for functional osteochondral regeneration. Biomaterials 2021;266:120385.
[30] Brennan CM, Eichholz KF, Hoey DA. The effect of pore size within fibrous scaffolds fabricated using melt electrowriting on human bone marrow stem cell osteogenesis. Biomedical materials (Bristol, England) 2019;14(6):065016.
[31] Aisenbrey EA, Tomaschke A, Kleinjan E, Muralidharan A, Pascual-Garrido C, McLeod RR, Ferguson VL, Bryant SJ. A stereolithography-based 3D printed hybrid scaffold for in situ cartilage defect repair. Macromol Biosci 2018;18(2):1700267.
[32] O'Connell CD, Duchi S, Onofrillo C, Caballero-Aguilar LM, Trengove A, Doyle SE, Zywicki WJ, Pirogova E, Di Bella C. Within or without you? A perspective comparing in situ and ex situ tissue engineering strategies for articular cartilage repair. Adv Healthc Mater 2022;11(24):e2201305.
[33] Samandari M, Mostafavi A, Quint J, Memić A, Tamayol A. In situ bioprinting: intraoperative implementation of regenerative medicine. Trends Biotechnol 2022;40(10):1229–47.
[34] Mahmoudi Z, Sedighi M, Jafari A, Naghieh S, Stefanek E, Akbari M, Savoji H. In situ 3D bioprinting: a promising technique in advanced biofabrication strategies. Bioprinting 2023:e00260.
[35] Guarnera D, Restaino F, Vannozzi L, Trucco D, Mazzocchi T, Worwąg M, Gapinski T, Lisignoli G, Zaffagnini S, Russo A, Ricotti L. Arthroscopic device with bendable tip for the controlled extrusion of hydrogels on cartilage defects. Sci Rep 2024;14:19904.
[36] Castilho M, van Mil A, Maher M, Metz CHG, Hochleitner G, Groll J, Doevendans PA, Ito K, Sluijter JPG, Malda J. Melt electrowriting allows tailored microstructural and mechanical design of scaffolds to advance functional human myocardial tissue formation. Adv Funct Mater 2018;28(40):1803151.
[37] Wang Y, Zhang Y, Zhang Z, Su Y, Wang Z, Dong M, Chen M. An injectable high-conductive bimaterial scaffold for neural stimulation. Colloids Surf B Biointerfaces 2020;195:111210.
[38] Nahm D, Weigl F, Schaefer N, Sancho A, Frank A, Groll J, Villmann C, Schmidt H-W, Dalton PD, Luxenhofer R. A versatile biomaterial ink platform for the melt electrowriting of chemically-crosslinked hydrogels. Mater Horiz 2020;7(3):928–33.
[39] Denier JP, Dabrowski PP. On the boundary–layer equations for power–law fluids. Proceedings of the Royal Society of London. Series A: Math Phys Eng Sci 2004;460(2051):3143–58.
[40] Palma JH, Bertuola M, Hermida ÉB. Modeling calcium diffusion and crosslinking dynamics in a thermogelling Alginate-Gelatin-Hyaluronic acid ink: 3D bioprinting applications. Bioprinting 2024;38:e00329.
[41] Coutinho DF, Sant SV, Shin H, Oliveira JT, Gomes ME, Neves NM, Khademhosseini A, Reis RL. Modified Gellan Gum hydrogels with tunable physical and mechanical properties. Biomaterials 2010;31(29):7494–502.
[42] Trucco D, Riacci L, Vannozzi L, Manferdini C, Arrico L, Gabusi E, Lisignoli G, Ricotti L. Primers for the adhesion of gellan gum-based hydrogels to the cartilage: a comparative study. Macromol Biosci 2022;22(10):2200096.
[43] Olvera D, Sohrabi Molina M, Hendy G, Monaghan MG. Electroconductive melt electrowritten patches matching the mechanical anisotropy of human myocardium. Adv Funct Mater 2020;30(44):1909880.
[44] S.J F, Mohd Yusof AA, Isa K, Harun M. The tendency of nature towards hexagon shape formation due to minimizing surface energy. International Journal of Integrated Engineering 2022;14:40–7.
[45] Amagat Molas J, Chen M. Injectable PLCL/gelatin core-shell nanofibers support noninvasive 3D delivery of stem cells. Int J Pharm 2019;568:118566.
[46] Xu C, Yang K, Xu Y, Meng X, Zhou Y, Xu Y, Li X, Qiao W, Shi J, Zhang D, Wang J, Xu W, Yang H, Luo Z, Dong N. Melt-electrowriting-enabled anisotropic scaffolds loaded with valve interstitial cells for heart valve tissue Engineering. J Nanobiotechnol 2024;22(1):378.
[47] de Ruijter M, Hrynevich A, Haigh JN, Hochleitner G, Castilho M, Groll J, Malda J, Dalton PD. Out-of-Plane 3D-printed microfibers improve the shear properties of hydrogel composites. Small 2018;14(8):1702773.
[48] Galarraga JH, Locke RC, Witherel CE, Stoeckl BD, Castilho M, Mauck RL, Malda J, Levato R, Burdick JA. Fabrication of MSC-laden composites of hyaluronic acid hydrogels reinforced with MEW scaffolds for cartilage repair. Biofabrication 2022;14(1):014106.
[49] Bas O, De-Juan-Pardo EM, Meinert C, D'Angella D, Baldwin JG, Bray LJ, Wellard RM, Kollmannsberger S, Rank E, Werner C, Klein TJ, Catelas I, Hutmacher DW. Biofabricated soft network composites for cartilage tissue engineering. Biofabrication 2017;9(2):025014.
[50] Bas O, De-Juan-Pardo EM, Chhaya MP, Wunner FM, Jeon JE, Klein TJ, Hutmacher DW. Enhancing structural integrity of hydrogels by using highly organised melt electrospun fibre constructs. Eur Polym J 2015;72:451–63.
[51] Größbacher G, Bartolf-Kopp M, Gergely C, Bernal PN, Florczak S, de Ruijter M, Rodriguez NG, Groll J, Malda J, Jungst T, Levato R. Volumetric printing across melt electrowritten scaffolds fabricates multi-material living constructs with tunable architecture and mechanics. Adv Mater 2023;35(32):2300756.
[52] Hafezi M, Nouri Khorasani S, Zare M, Esmaeely Neisiany R, Davoodi P. Advanced hydrogels for cartilage tissue engineering: recent progress and future directions. Polymers 2021;13(23).
[53] Chao CK, Lin SY. Failure stability of a cracked layer between dissimilar materials. Theor Appl Fract Mech 1990;13(1):59–68.
[54] Manferdini C, Trucco D, Saleh Y, Gabusi E, Dolzani P, Lenzi E, Vannozzi L, Ricotti L, Lisignoli G. RGD-functionalized hydrogel supports the chondrogenic commitment of adipose mesenchymal stromal cells. Gels 2022;8(6):382.

[55] Costa JB, Pereira H, Espregueira-Mendes J, Khang G, Oliveira JM, Reis RL. Tissue engineering in orthopaedic sports medicine: current concepts. Journal of ISAKOS: Joint Disorders & Orthopaedic Sports Medicine 2017;2(2):60–6.
[56] Lee SC, Gillispie G, Prim P, Lee SJ. Physical and chemical factors influencing the printability of hydrogel-based extrusion bioinks. Chem Rev 2020;120(19): 10834–86.
[57] Moo EK, Ebrahimi M, Hrynevich A, de Ruijter M, Castilho M, Malda J, Korhonen RK. Load-induced fluid pressurisation in hydrogel systems before and after reinforcement by melt-electrowritten fibrous meshes. Journal of the mechanical behavior of biomedical materials 2023;143:105941.